Direct Measurement of the Cosmic-Ray Carbon and Oxygen spectra from 10 GeV/n to 2.2 TeV/n with the Calorimetric Electron Telescope on the International Space Station

SUPPLEMENTAL MATERIAL

(CALET collaboration)

Supplemental material concerning "Direct Measurement of the Cosmic-Ray Carbon and Oxygen spectra from 10 GeV/n to 2.2 TeV/n with the Calorimetric Electron Telescope on the International Space Station"

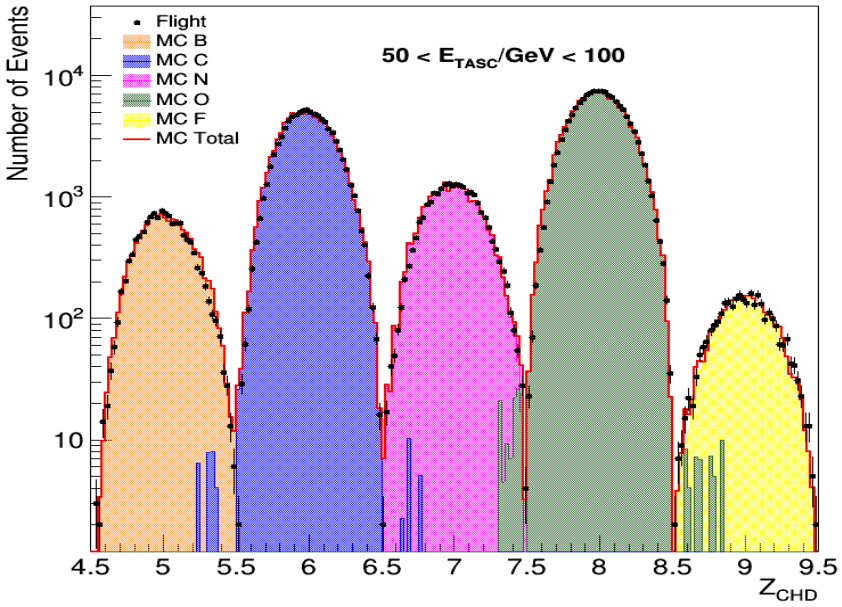

(a)

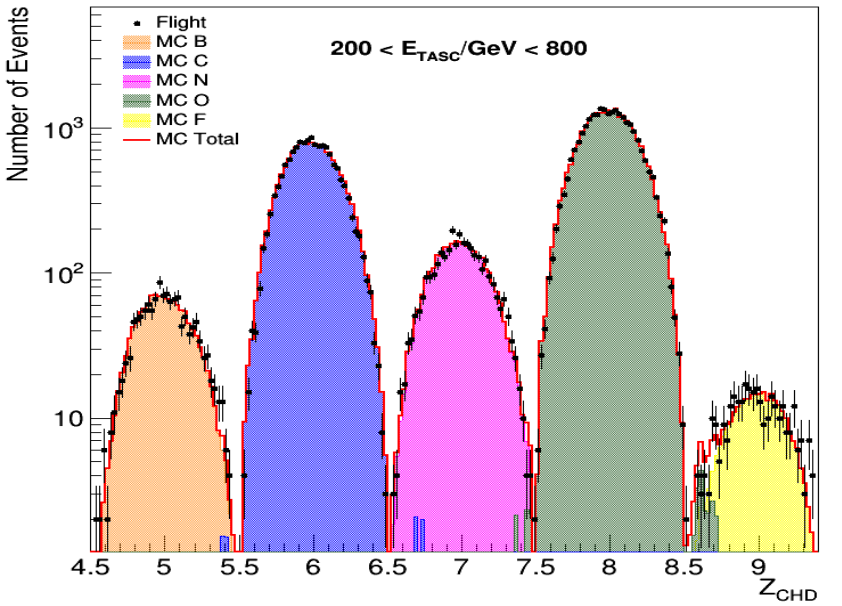

(b)

FIG. S1. Charge distributions from the combined CHD layers in the elemental region between B and F. Events are selected with (a) $50 < E_{\mathrm{TASC}} < 100$ GeV and (b) $200 < E_{\mathrm{TASC}} < 800$ GeV and a measured charge in IMC consistent with Z_{CHD}. FD (black dots) are compared to MC samples. The distributions shown in these plots are only representative of the charge resolution while the relative elemental abundances are not meaningful, because of the different trigger efficiency for different nuclear species (Fig. S7) and different intervals of primary energy per nucleon selected.

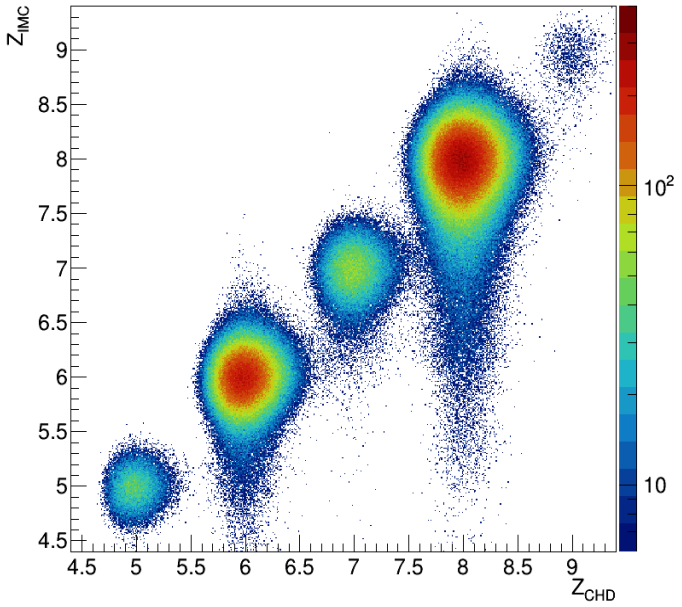

FIG. S2. Crossplot of IMC versus CHD reconstructed charges in the elemental range between B and F. Events with C and O nuclei undergoing a charge-changing nuclear interaction upstream the IMC are clearly visible in the tail of their drop-shaped distributions extending to lower Z_{IMC} values. These events are removed in the analysis by requiring the consistency, within 30%, between the mean values of dE/dx measurements in the first four layers in each IMC view and then by applying a window cut to Z_{IMC} of half-width $2\sigma_Z$ centered around the nominal charge values.

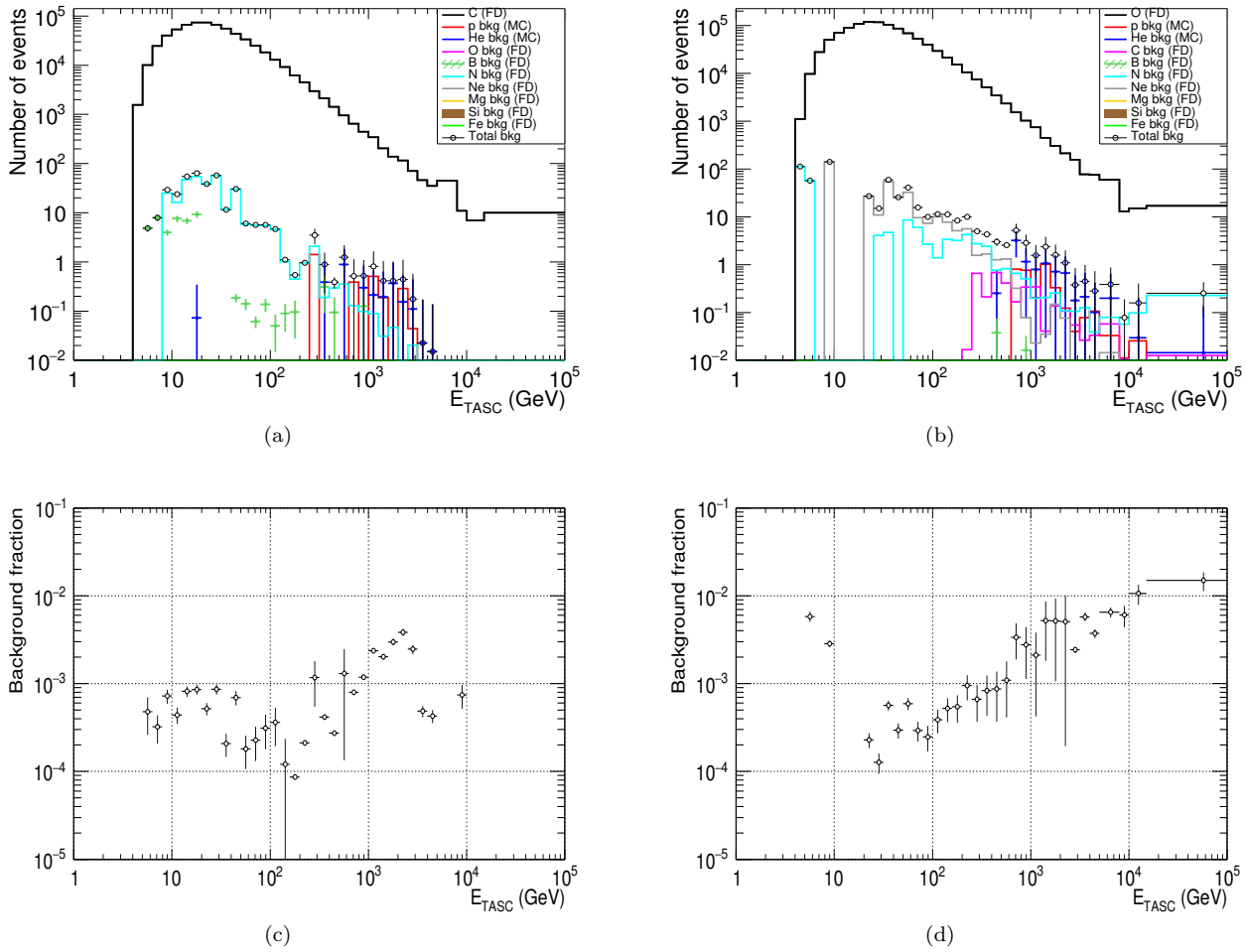

FIG. S3. Distributions of E_{TASC} for selected carbon (a) and oxygen (b) events in FD (black line) and estimated contamination from different nuclei. The total background (open black dots) fraction as a function of E_{TASC} is shown for (c) carbon and (d) oxygen. Contamination of each nuclear species with $Z > 4$ is estimated by rescaling its E_{TASC} distribution measured in FD by the ratio, estimated with MC simulations, of its reconstruction efficiency to the probability of being misidentified as C or O. Background due to proton and helium is computed by normalizing their E_{TASC} distributions from MC to the number of events expected from previous flux measurements.

ENERGY MEASUREMENT

Differently from the case of electrons, the energy released in TASC by interacting CR nuclei is only a fraction of the primary particle energy, the electromagnetic component of the hadronic cascades, originating from the decays of π^0 secondaries produced in the showers. Though a significant part of the hadronic cascade energy leaks out of the calorimeter because of its limited thickness (1.3 λ_I), the energy deposited in the TASC by the electromagnetic shower core scales linearly with the incident particle energy, albeit with large event-to-event fluctuations. As a result, the energy resolution is poor by the standards of total containment hadron calorimetry in experiments at accelerators. Nevertheless, it is sufficient to reconstruct the steep energy spectra of CR nuclei with a nearly energy independent resolution.

The TASC response to nuclei was studied at CERN SPS in 2015 using a beam of accelerated ion fragments with $A/Z = 2$ and kinetic energy of 13, 19 and 150 GeV/n [S1]. In Fig. S4a, the $E_{\rm TASC}$ distributions for C nuclei at 150 GeV/n is shown as an example. C nuclei in the beam are selected with CHD and the HE trigger is applied. The resulting distribution looks nearly gaussian, the energy released in the TASC is ∼20% of the particle energy and the resolution σ_E is close to 30%. The mean energy deposited in TASC by different nuclear species in the beam (selected with CHD) is plotted as a function of the kinetic energy per particle in Fig. S4b. The energy response of TASC is linear up to the maximum available particle energy of 6 TeV (obtained with a primary beam of ^{40}Ar nuclei).

The energy response derived from MC simulations was tuned using the beam test results. Correction factors are 6.7% for $E_{\rm TASC} < 45$ GeV and 3.5% for $E_{\rm TASC} > 350$ GeV, respectively, while a simple linear interpolation is used to determine the correction factor for intermediate energies.

For flux measurement, energy unfolding is applied to correct $E_{\rm TASC}$ distributions of selected C and O candidates for significant bin-to-bin migration effects (due to the limited energy resolution) and infer the primary particle energy. In this analysis, we apply the iterative unfolding method based on the Bayes' theorem [S2] implemented in the RooUnfold package [S3, S4]. The response matrix is derived using MC simulations of the CALET flight model after applying the same selection as for FD and used in the unfolding procedure (Fig. S5). Each element of the matrix represents the probability that primary nuclei in a certain energy interval of the CR spectrum produce an energy deposit in a given $E_{\rm TASC}$ bin.

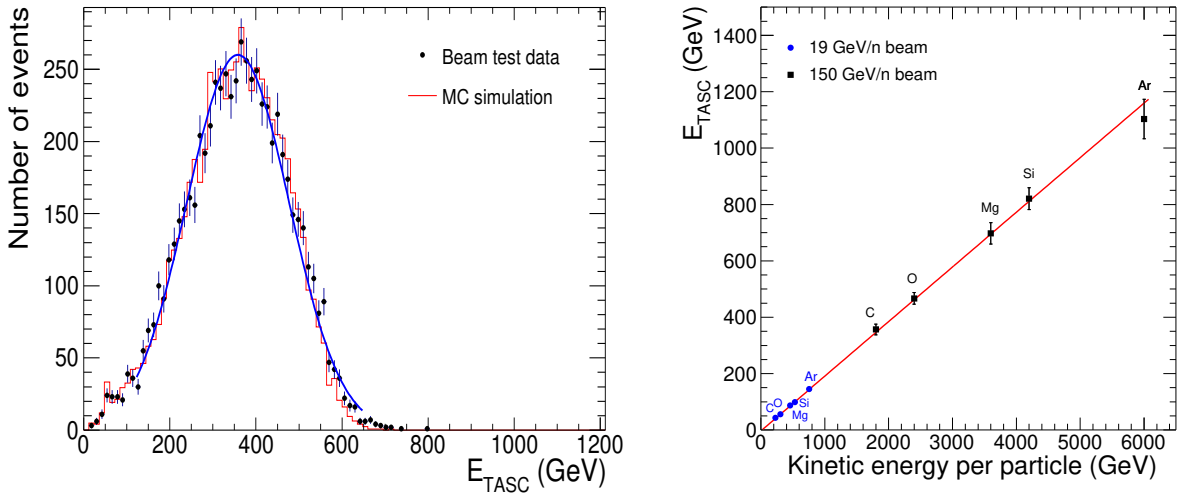

(a) (b)

FIG. S4. (a) Energy deposited in TASC by a beam of accelerated C nuclei of fixed energy 150 GeV/n at CERN-SPS [S1]. The data are fitted to a gaussian (blue line); the mean value is 20% of the kinetic beam particle energy, and the energy resolution (defined as the standard deviation to mean ratio) is ∼30%. (b) Energy linearity of TASC as measured at CERN SPS with beams of 19 (blue dots) and 150 (black squares) GeV/n ion fragments with $A/Z = 2$. The red line represents a linear fit to the data. The fitted slope is 0.194 ± 0.005, indicating that on average ∼20% of the particle energy is deposited in TASC.

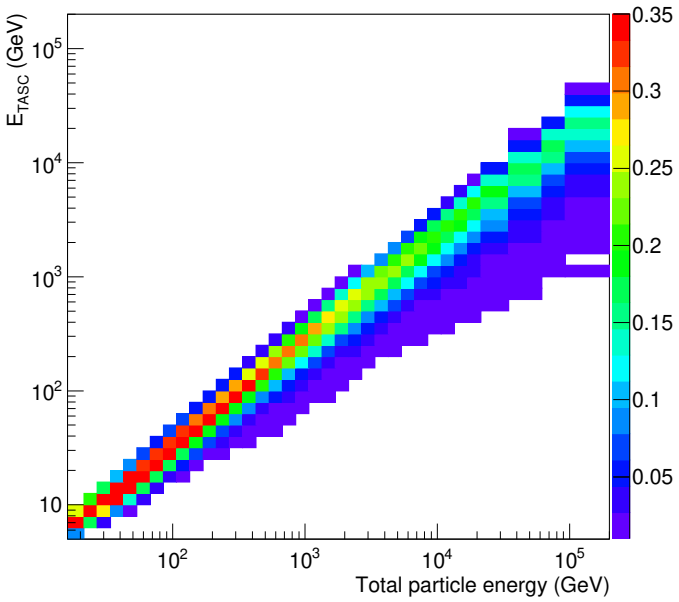

FIG. S5. Response matrix for oxygen derived from MC simulations of the CALET flight model by applying the same selection as for FD. The color scale is associated to the probability that nuclei of a given energy produce showers in different intervals of E_{TASC}.

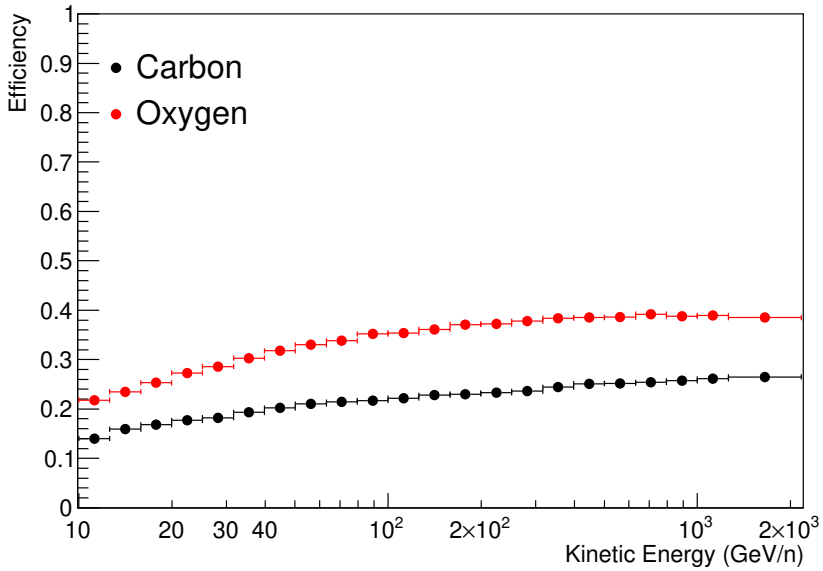

FIG. S6. Total selection efficiency for C (black dots) and O (red dots) estimated with MC simulations.

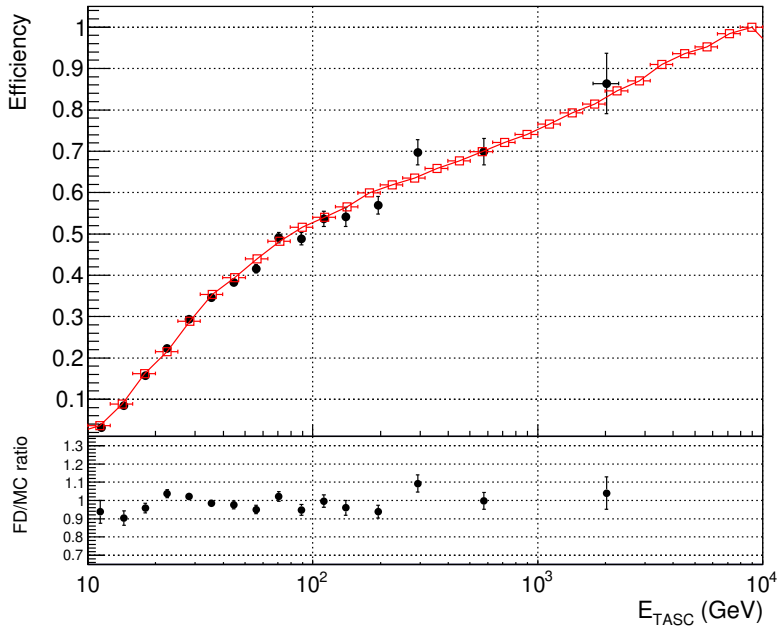

(a)

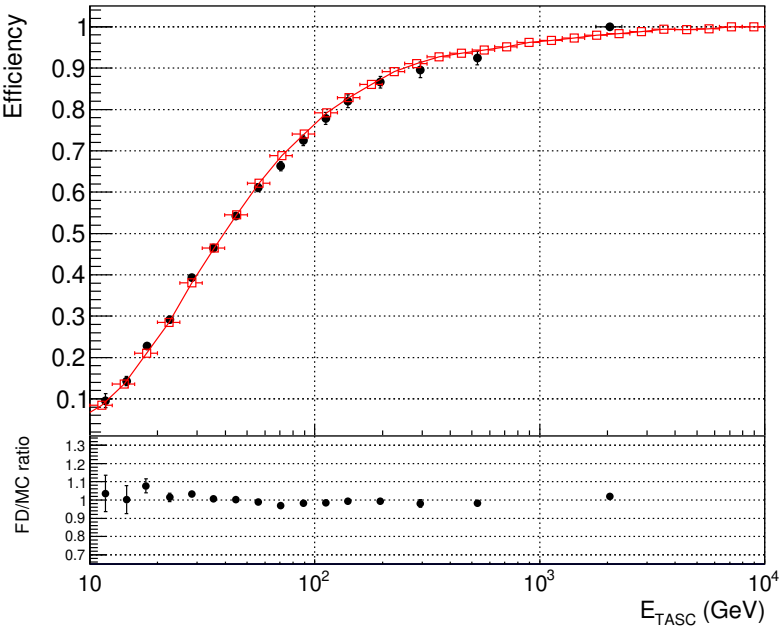

(b)

FIG. S7. HE trigger efficiency as a function of the deposited energy in TASC for C (*a*) and O (*b*) as derived from flight data (FD) (black dots) and Monte Carlo (MC) (red rectangles). The FD to MC efficiency ratio is shown in the lower canvas. The HE trigger efficiency was measured directly from the data by using dedicated runs where in addition to HE, a low-energy (LE) trigger was active. The trigger logic is the same for both trigger (i.e. coincidence of the pulse heights of the last two pairs of IMC layers and the top TASC layer) but lower discriminator thresholds are set for the input signals in case of LE trigger, allowing to trigger also penetrating nuclei with $Z > 2$. The ratio of the number of events counted by both triggers to those registered by the LE trigger only is an estimate of the HE trigger efficiency in each bin of deposited energy. To compare with simulations, we apply exactly the same method to MC samples, where both trigger modes are modeled.

SURVIVAL PROBABILITIES

In order to check that hadronic interactions in the detector are well simulated, we have measured the survival probabilities of C and O nuclei at different depths in IMC and compared with the ones expected from MC simulations. For each HE-triggered event, selected as C or O by means of CHD only, several measurements of the charge are obtained by dE/dx samples along the particle track in pairs of adjacent scintillating-fiber (SciFi) layers. The coupled SciFi layers are spaced by about 2.3 cm and interleaved with W plates (except for the first pair), aluminum honeycomb panels and CFRP (carbon fiber reinforced polymer) supporting structures. From the charge distribution of each pair of Scifi layers, the number of events that did not interact in the material upstream the fibers can be estimated by selecting the nuclei with a charge value consistent with the one measured in CHD. The reduction in the number of not-interacted events, normalized to the ones selected in CHD, allows to measure the survival probability as a function of the material thickness traversed by the particle in the IMC, as shown in Fig. S8. In MC data, the survival probabilities can be calculated by using the true information on the point where the first hadronic interaction occurs in the detector. The survival probabilities measured in FD are in good agreement (within $< 1\%$) with MC predictions, as shown in the bottom panels of Fig. S8.

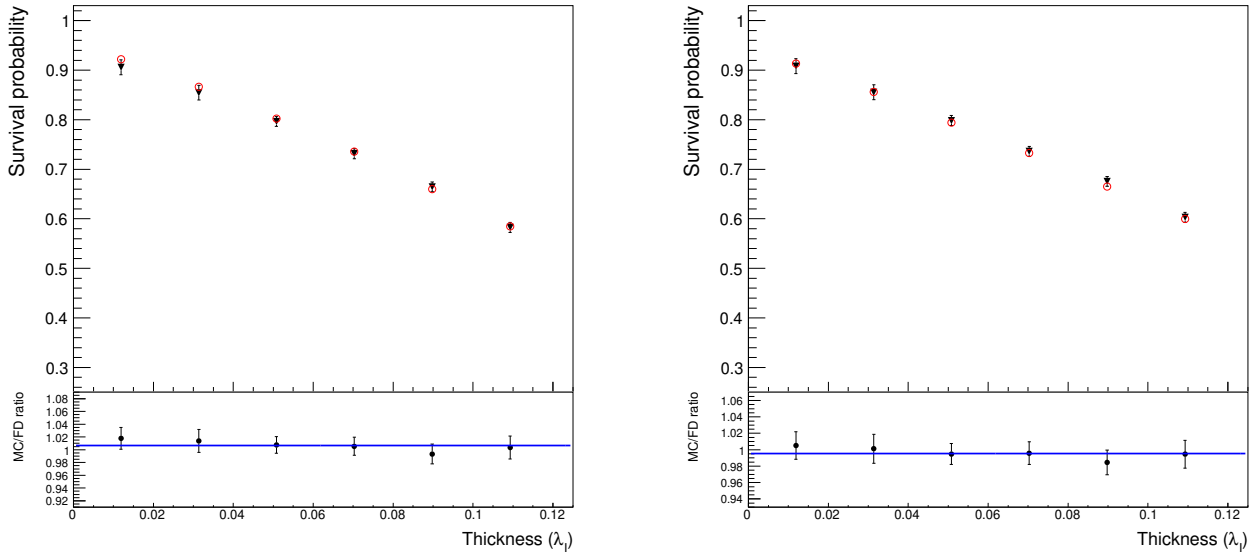

(a) (b)

FIG. S8. Survival probability as a function of the material thickness traversed by the particles in IMC as derived from FD (black triangles) and MC (red circles) for carbon (*a*) and oxygen (*b*) (upper panels). The survival probabilities are calculated in FD by dividing the number of events selected as C (O) in the first six pairs of SciFi layers in IMC by the number of C (O) events selected with CHD. The material thickness is expressed in units of proton interaction length λ_I and it is measured from the bottom of CHD. The coupled SciFi layers are preceded by 0.2 X_0-thick W plates (except the first pair), Al honeycomb panels and CFRP supporting structures. In bottom panels, the blue dotted line represents a constant value fitted to the ratio between MC and FD survival probabilities. The fitted value is 0.997 ± 0.008 (1.006 ± 0.006) for O (C).

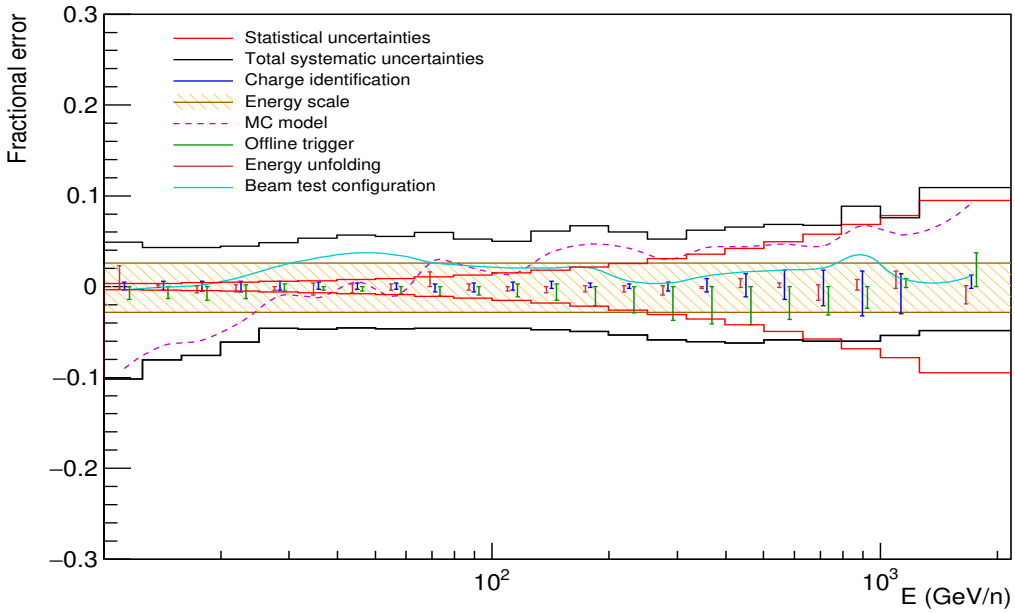

(a)

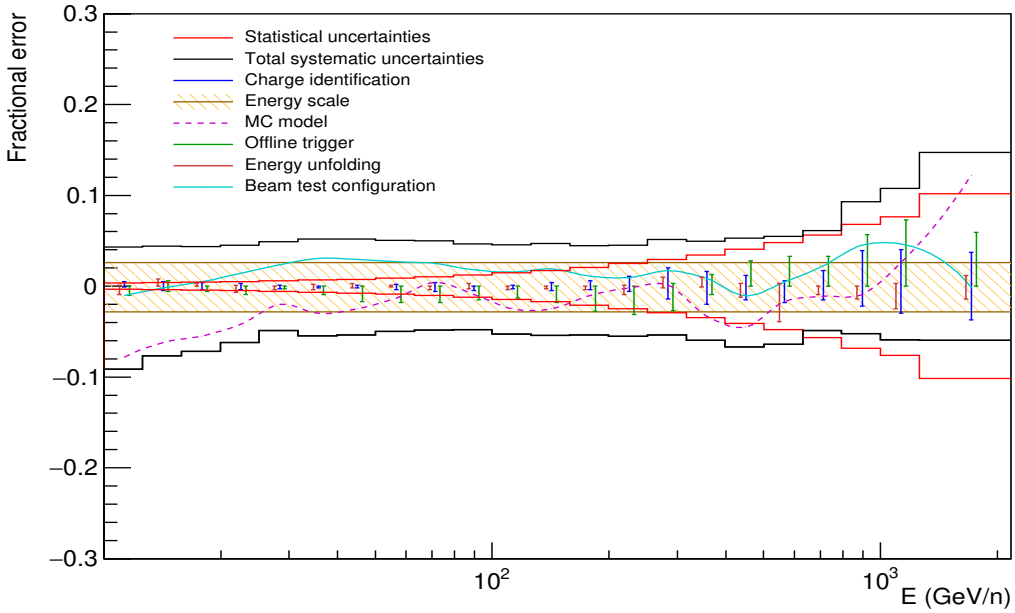

(b)

FIG. S9. Energy (per nucleon in GeV) dependence of systematic uncertainties (relative errors) for C (*a*) and O (*b*). The band defined by the red lines represents the statistical error in each energy bin. The band within the black lines shows the sum in quadrature of all the sources of systematics. A detailed breakdown of systematic errors, stemming from charge identification, offline trigger, MC model, energy scale correction, energy unfolding and beam test configuration, is shown.

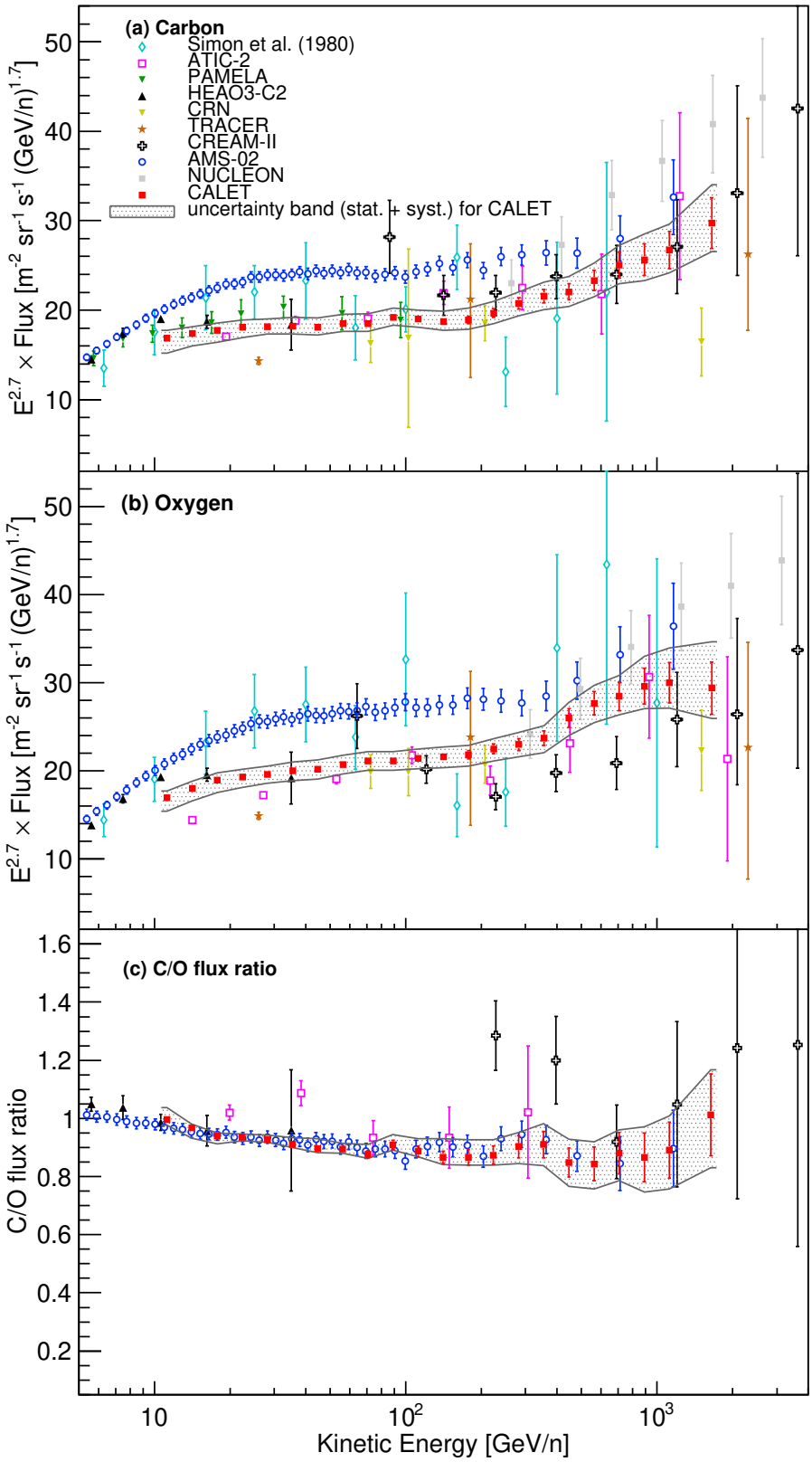

FIG. S10. CALET (a) carbon and (b) oxygen flux (multiplied by $E^{2.7}$) and (c) ratio of carbon to oxygen fluxes, as a function of kinetic energy E. Error bars of CALET data (red) represent the statistical uncertainty only, while the gray band indicates the quadratic sum of statistical and systematic errors. Also plotted are other direct measurements [S5–S13].

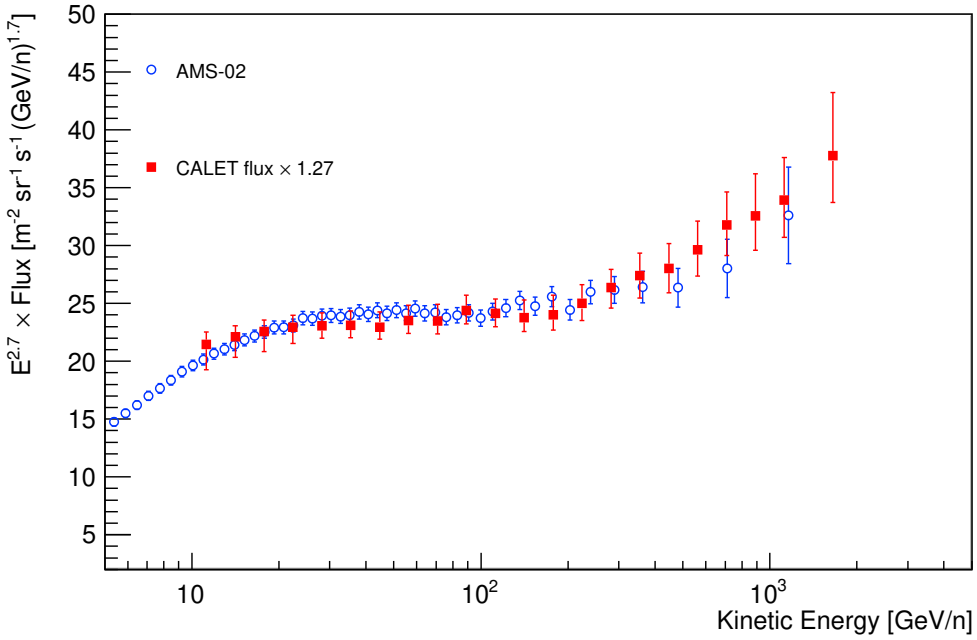

(a)

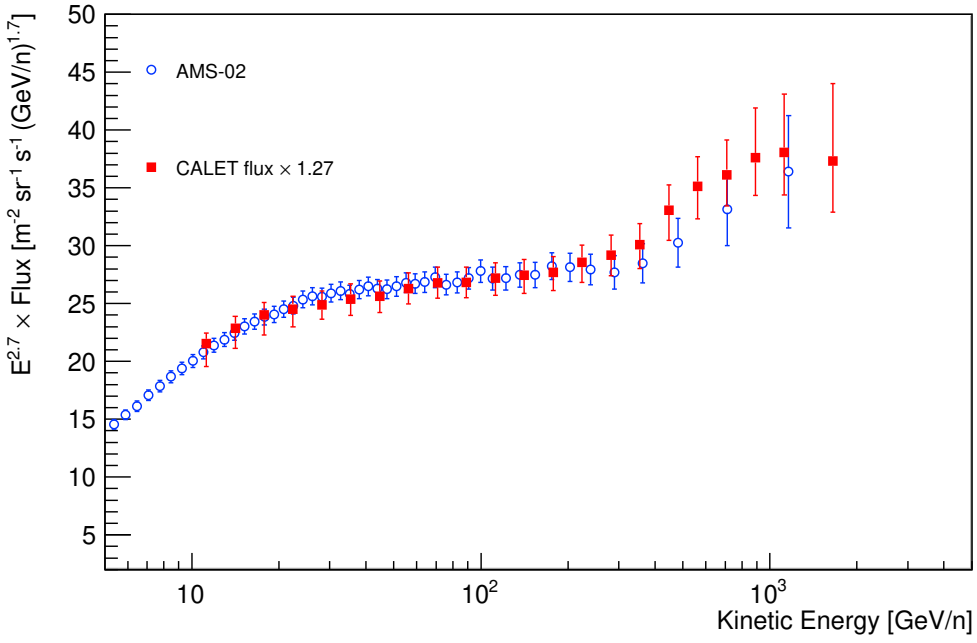

(b)

FIG. S11. (*a*) Carbon and (*b*) oxygen fluxes measured by CALET (red points) are multiplied by 1.27 for comparison with AMS-02 results [S5]. Error bars of CALET data represent the quadratic sum of statistical and systematic uncertainties. The factor (1.27±0.03) is obtained by a simultaneous minimization of the sum of squared residuals between CALET and AMS data points for C and O.

SPECTRAL FIT METHOD

We have tested two models for the C and O energy spectra: a double power-law (DPL) in energy

$$\Phi(E) = \begin{cases} C\left(\frac{E}{\mathrm{GeV}}\right)^{\gamma} & E \leq E_0 \\ C\left(\frac{E}{\mathrm{GeV}}\right)^{\gamma}\left(\frac{E}{E_0}\right)^{\Delta\gamma} & E > E_0 \end{cases} \tag{S1}$$

and a single power-law (SPL)

$$\Phi(E) = C\left(\frac{E}{\mathrm{GeV}}\right)^{\gamma} \tag{S2}$$

where C is a normalization factor, γ the spectral index, and $\Delta\gamma$ the spectral index change above the transition energy E_0. We have fitted the data using a chi-square minimization. The effect of systematic uncertainties in the measurement of the energy spectrum is modeled introducing in the χ^2 function a set of nuisance parameters.
The χ^2 function is defined as

$$\chi^2 = \sum_{i=4}^{N}\left[\frac{\Phi_i + S(E_i,\boldsymbol{\beta})\sigma_i^{sys} - \Phi(E_i,\mathbf{p})}{\sigma_i^{stat}}\right]^2 + \sum_{j=1}^{N_{np}}\beta_i^2 \tag{S3}$$

where Φ_i, σ_i^{stat}, σ_i^{sys}, E_i are the measured flux, the statistical and systematic errors, and the energy of the i-th bin (geometric mean of bin edges), respectively; $N = 22$ is the number of data points and the fit starts from the fourth point. The elements of the vector $\mathbf{p}$ are the free parameters of the model function Φ used in the fit: $\mathbf{p} = \{C, \gamma, \Delta\gamma, E_0\}$ for Eq. S1, and $\mathbf{p} = \{C, \gamma\}$ for Eq. S2.
$\boldsymbol{\beta}$ is a set of independent nuisance parameters β_j with $j = 1, ..., N_{np}$ introduced to properly account for systematic uncertainties in the fit. The energy range to be fitted (from 25 to 2200 GeV/n) is logarithmically divided into N_{np} intervals. According to the energy dependence of the systematic fractional errors (Fig. S9), we chose $N_{np} = 6$; therefore the width of each interval covers three consecutive energy bins of the spectrum. A nuisance parameter β_j is assigned to each interval. In the fit, a gaussian constraint (the last term in Eq. S3) is applied to each parameter β_j, with zero mean and standard deviation equal to 1. In the χ^2 function, the systematic errors σ_i^{sys} are multiplied by a piece-wise function $S(E_i, \boldsymbol{\beta})$, which assumes the value of β_j of the corresponding energy interval within which E_i falls.
The results of the fits with the two models are shown in Figs. S12 and S13 for C and O spectrum, respectively. We also performed the fits by varying the number of nuisance parameters, with similar results and significance.

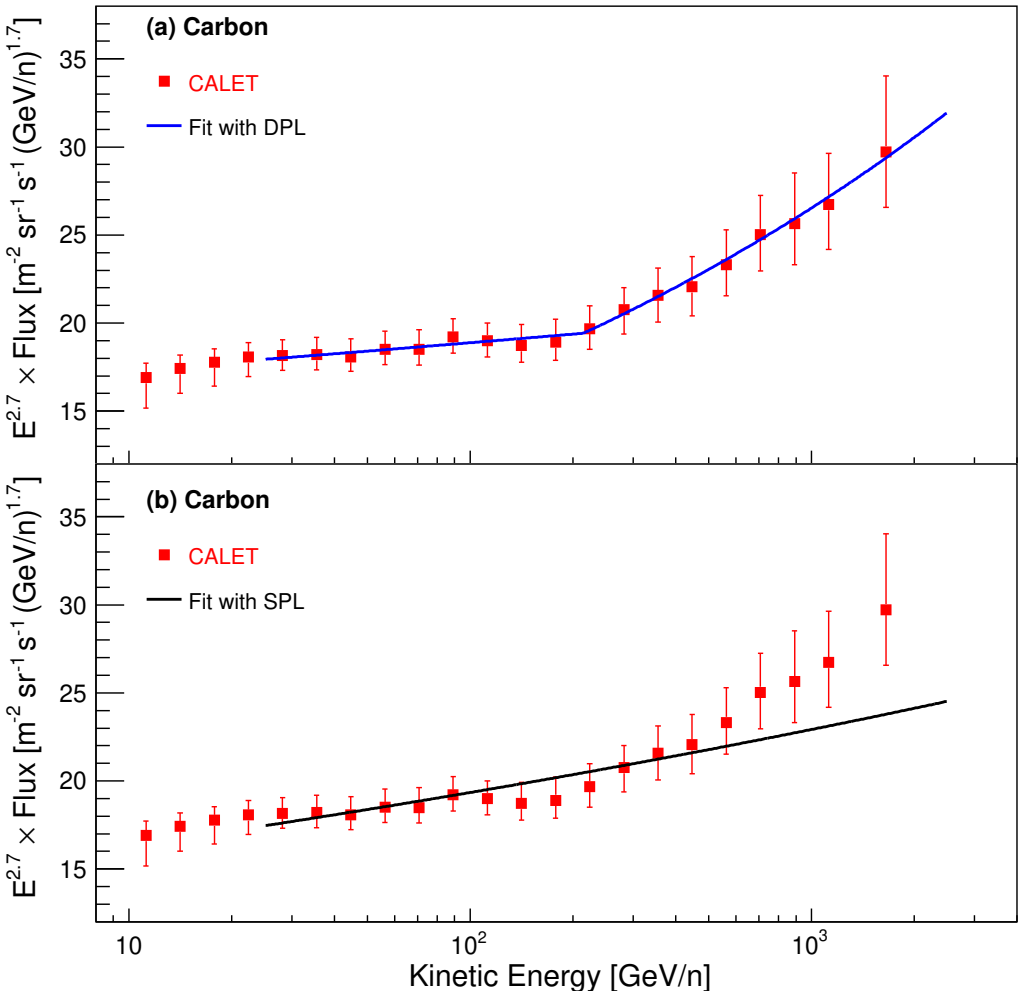

FIG. S12. Fit to the carbon energy spectrum with (a) a DPL function (Eq. S1) and (b) a SPL function (Eq. S2), in the energy range [25, 2000] GeV/n. Error bars of CALET data points represent the sum in quadrature of statistical and systematic uncertainties. The DPL fit yields $\gamma = -2.663 \pm 0.014$, $E_0 = (215 \pm 54)$ GeV/n, $\Delta\gamma = 0.166 \pm 0.042$, with χ^2/d.o.f. $= 9.0/8$. The SPL fit yields $\gamma = -2.626 \pm 0.010$ with χ^2/d.o.f. $= 27.5/10$. The difference $\Delta\chi^2 = 18.5$ between the fits with the two models, with two additional free parameters in DPL fit with respect to SPL fit, allows to exclude the single power law hypothesis at the 3.9σ level.

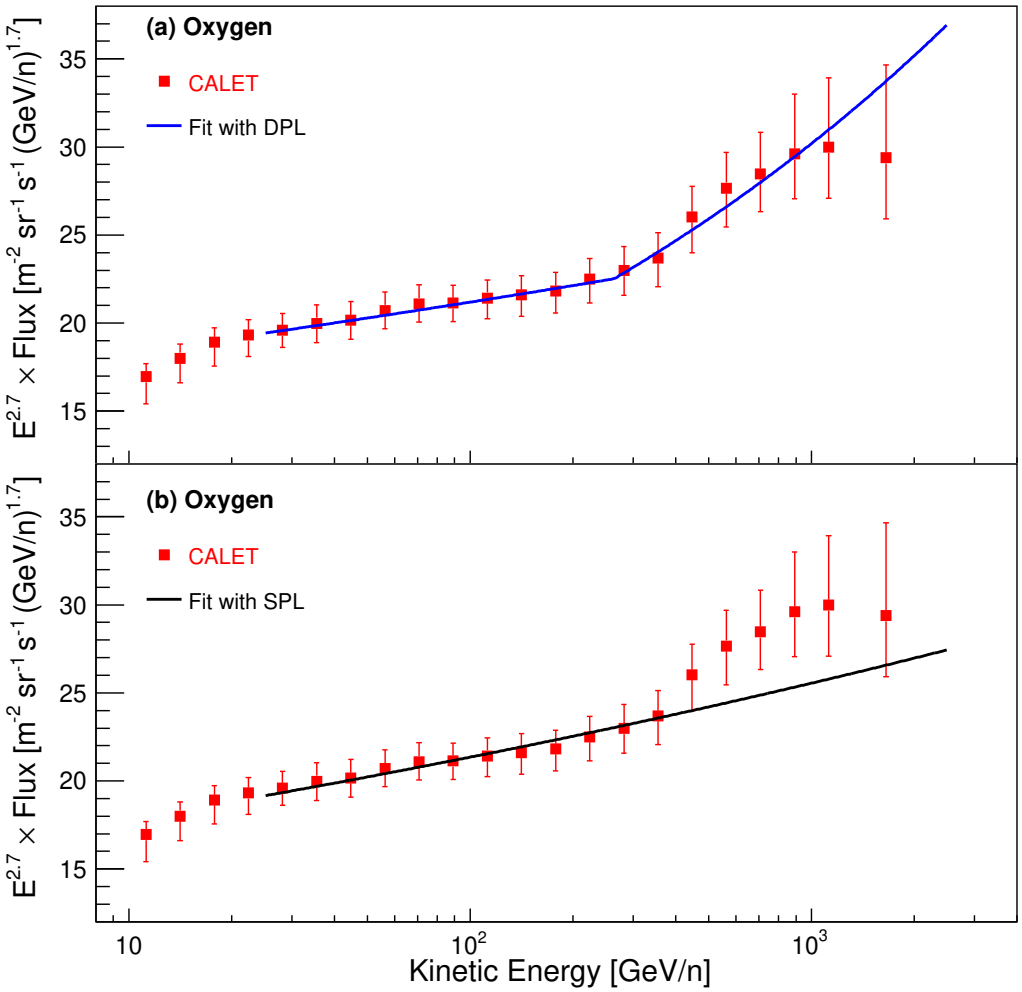

FIG. S13. Fit to the oxygen energy spectrum with (a) a DPL function (Eq. S1) and (b) a SPL function (Eq. S2), in the energy range [25, 2000] GeV/n. Error bars of CALET data points represent the sum in quadrature of statistical and systematic uncertainties. The DPL fit yields $\gamma = -2.637 \pm 0.009$, $E_0 = (264 \pm 53)$ GeV/n, $\Delta\gamma = 0.158 \pm 0.053$, with χ^2/d.o.f. $= 3.0/8$. The SPL fit yields $\gamma = -2.622 \pm 0.008$ with χ^2/d.o.f. $= 15.9/10$. The difference $\Delta\chi^2 = 12.9$ between the fits with the two models, with two additional free parameters in DPL fit with respect to SPL fit, allows to exclude the single power law hypothesis at the 3.2σ level.

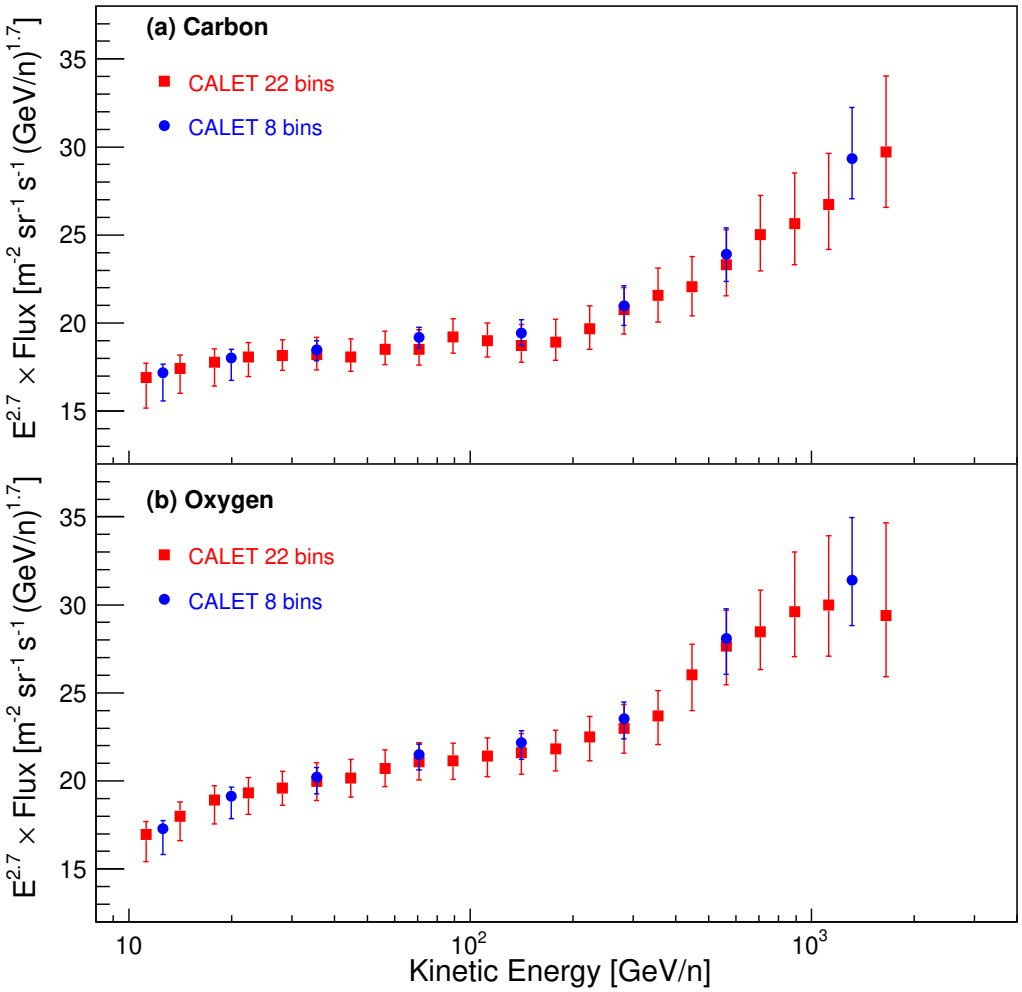

FIG. S14. CALET carbon (a) and oxygen (b) spectra derived with two different energy binnings. In the reference spectra (red squares) the energy range from 10 GeV/n to 2.2 TeV/n is divided into 22 bins (Tables I and II); all bins are chosen to have relative width commensurate with the TASC energy resolution σ_E, with the exception of the last bin whose width is $2 \times \sigma_E$. To study possible binning related effects in the spectra, C and O fluxes are also derived by dividing the energy range into 8 bins (blue dots), with relative bin width $\sim 2.5 \times \sigma_E$, but the last bin whose width is $3.5 \times \sigma_E$. The wide-bin spectra have the same shape as the original ones. The flux differences are well within the error bars, representing the quadratic sum of of statistical and systematic uncertainties.

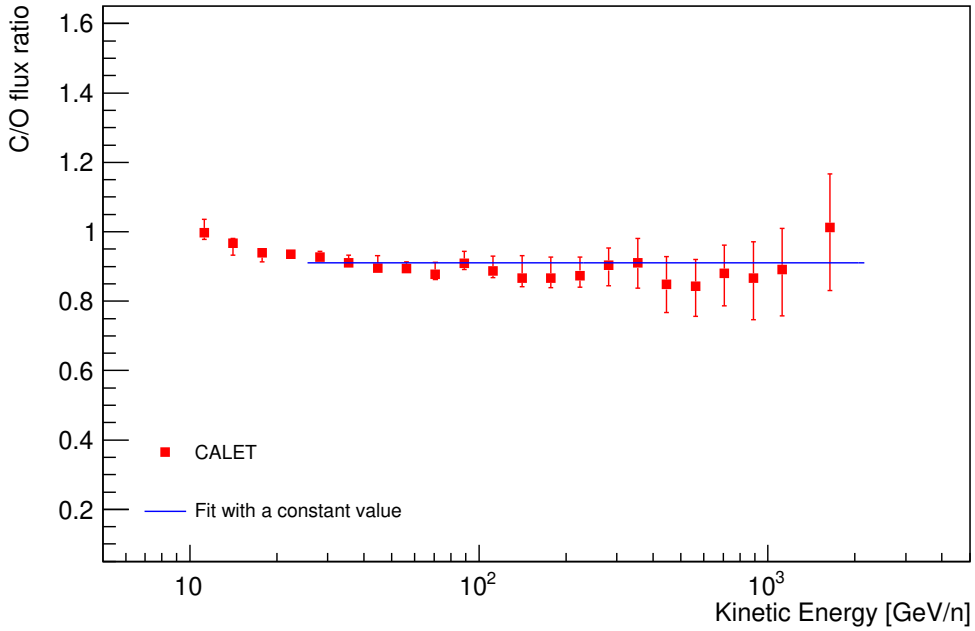

FIG. S15. The carbon to oxygen flux ratio as a function of kinetic energy per nucleon is fitted to a constant function (blue line). Error bars of CALET data points represent the sum in quadrature of statistical and systematic uncertainties. Above 25 GeV/n the C/O ratio is described by a constant value of 0.911 ± 0.006 with χ^2/d.o.f. $= 8.3/17$.

TABLE I. Table of CALET carbon spectrum. The first, second and third error in the flux represents the statistical uncertainties, systematic uncertainties in normalization, and energy dependent systematic uncertainties, respectively.

Energy Bin [GeV/n]	Flux [$\mathrm{m^{-2}sr^{-1}s^{-1}(GeV/}n\mathrm{)^{-1}}$]
10.0–12.6	$(2.471 \pm 0.008\,^{+0.106}_{-0.110}\,^{+0.058}_{-0.226}) \times 10^{-2}$
12.6–15.8	$(1.368 \pm 0.005\,^{+0.059}_{-0.061}\,^{+0.009}_{-0.092}) \times 10^{-2}$
15.8–20.0	$(7.492 \pm 0.032\,^{+0.321}_{-0.332}\,^{+0.047}_{-0.461}) \times 10^{-3}$
20.0–25.1	$(4.092 \pm 0.020\,^{+0.175}_{-0.182}\,^{+0.051}_{-0.172}) \times 10^{-3}$
25.1–31.6	$(2.208 \pm 0.013\,^{+0.095}_{-0.098}\,^{+0.051}_{-0.028}) \times 10^{-3}$
31.6–39.8	$(1.189 \pm 0.008\,^{+0.051}_{-0.053}\,^{+0.038}_{-0.019}) \times 10^{-3}$
39.8–50.1	$(6.341 \pm 0.049\,^{+0.271}_{-0.281}\,^{+0.236}_{-0.058}) \times 10^{-4}$
50.1–63.1	$(3.487 \pm 0.031\,^{+0.149}_{-0.155}\,^{+0.122}_{-0.048}) \times 10^{-4}$
63.1–79.4	$(1.871 \pm 0.020\,^{+0.080}_{-0.083}\,^{+0.078}_{-0.022}) \times 10^{-4}$
79.4–100.0	$(1.044 \pm 0.013\,^{+0.045}_{-0.046}\,^{+0.031}_{-0.012}) \times 10^{-4}$
100.0–125.9	$(5.545 \pm 0.084\,^{+0.237}_{-0.246}\,^{+0.141}_{-0.071}) \times 10^{-5}$
125.9–158.5	$(2.932 \pm 0.053\,^{+0.125}_{-0.130}\,^{+0.128}_{-0.049}) \times 10^{-5}$
158.5–199.5	$(1.590 \pm 0.034\,^{+0.068}_{-0.071}\,^{+0.082}_{-0.035}) \times 10^{-5}$
199.5–251.2	$(8.890 \pm 0.228\,^{+0.381}_{-0.394}\,^{+0.378}_{-0.264}) \times 10^{-6}$
251.2–316.2	$(5.035 \pm 0.154\,^{+0.216}_{-0.223}\,^{+0.154}_{-0.193}) \times 10^{-6}$
316.2–398.1	$(2.812 \pm 0.100\,^{+0.120}_{-0.125}\,^{+0.127}_{-0.117}) \times 10^{-6}$
398.1–501.2	$(1.544 \pm 0.065\,^{+0.066}_{-0.068}\,^{+0.076}_{-0.067}) \times 10^{-6}$
501.2–631.0	$(8.766 \pm 0.432\,^{+0.375}_{-0.389}\,^{+0.468}_{-0.339}) \times 10^{-7}$
631.0–794.3	$(5.053 \pm 0.292\,^{+0.216}_{-0.224}\,^{+0.264}_{-0.204}) \times 10^{-7}$
794.3–1000.0	$(2.780 \pm 0.190\,^{+0.119}_{-0.123}\,^{+0.215}_{-0.112}) \times 10^{-7}$
1000.0–1258.9	$(1.555 \pm 0.122\,^{+0.067}_{-0.069}\,^{+0.097}_{-0.047}) \times 10^{-7}$
1258.9–2166.7	$(6.094 \pm 0.578\,^{+0.261}_{-0.270}\,^{+0.613}_{-0.116}) \times 10^{-8}$

TABLE II. Table of CALET oxygen spectrum. The first, second and third error in the flux represents the statistical uncertainties, systematic uncertainties in normalization, and energy dependent systematic uncertainties, respectively.

Energy Bin [GeV/n]	Flux [$\mathrm{m^{-2}sr^{-1}s^{-1}(GeV/}n\mathrm{)^{-1}}$]
10.0–12.6	$(2.479 \pm 0.009\,^{+0.106}_{-0.110}\,^{+0.013}_{-0.198}) \times 10^{-2}$
12.6–15.8	$(1.414 \pm 0.005\,^{+0.061}_{-0.063}\,^{+0.016}_{-0.088}) \times 10^{-2}$
15.8–20.0	$(7.977 \pm 0.035\,^{+0.341}_{-0.354}\,^{+0.056}_{-0.450}) \times 10^{-3}$
20.0–25.1	$(4.374 \pm 0.022\,^{+0.187}_{-0.194}\,^{+0.063}_{-0.191}) \times 10^{-3}$
25.1–31.6	$(2.381 \pm 0.014\,^{+0.102}_{-0.106}\,^{+0.056}_{-0.050}) \times 10^{-3}$
31.6–39.8	$(1.305 \pm 0.009\,^{+0.056}_{-0.058}\,^{+0.039}_{-0.041}) \times 10^{-3}$
39.8–50.1	$(7.074 \pm 0.054\,^{+0.303}_{-0.314}\,^{+0.210}_{-0.215}) \times 10^{-4}$
50.1–63.1	$(3.901 \pm 0.035\,^{+0.167}_{-0.173}\,^{+0.106}_{-0.088}) \times 10^{-4}$
63.1–79.4	$(2.134 \pm 0.022\,^{+0.091}_{-0.095}\,^{+0.055}_{-0.041}) \times 10^{-4}$
79.4–100.0	$(1.148 \pm 0.014\,^{+0.049}_{-0.051}\,^{+0.021}_{-0.021}) \times 10^{-4}$
100.0–125.9	$(6.250 \pm 0.092\,^{+0.267}_{-0.277}\,^{+0.097}_{-0.179}) \times 10^{-5}$
125.9–158.5	$(3.384 \pm 0.058\,^{+0.145}_{-0.150}\,^{+0.066}_{-0.106}) \times 10^{-5}$
158.5–199.5	$(1.836 \pm 0.038\,^{+0.079}_{-0.081}\,^{+0.023}_{-0.056}) \times 10^{-5}$
199.5–251.2	$(1.017 \pm 0.025\,^{+0.044}_{-0.045}\,^{+0.015}_{-0.033}) \times 10^{-5}$
251.2–316.2	$(5.577 \pm 0.164\,^{+0.239}_{-0.247}\,^{+0.158}_{-0.170}) \times 10^{-6}$
316.2–398.1	$(3.088 \pm 0.106\,^{+0.132}_{-0.137}\,^{+0.075}_{-0.122}) \times 10^{-6}$
398.1–501.2	$(1.821 \pm 0.074\,^{+0.078}_{-0.081}\,^{+0.056}_{-0.091}) \times 10^{-6}$
501.2–631.0	$(1.040 \pm 0.050\,^{+0.045}_{-0.046}\,^{+0.035}_{-0.048}) \times 10^{-6}$
631.0–794.3	$(5.744 \pm 0.324\,^{+0.246}_{-0.255}\,^{+0.249}_{-0.119}) \times 10^{-7}$
794.3–1000.0	$(3.209 \pm 0.219\,^{+0.137}_{-0.142}\,^{+0.265}_{-0.089}) \times 10^{-7}$
1000.0–1258.9	$(1.745 \pm 0.133\,^{+0.075}_{-0.077}\,^{+0.173}_{-0.068}) \times 10^{-7}$
1258.9–2166.7	$(6.022 \pm 0.613\,^{+0.258}_{-0.267}\,^{+0.849}_{-0.238}) \times 10^{-8}$

TABLE III. Table of CALET carbon to oxygen flux ratio. The first and second error represents the statistical uncertainties and systematic uncertainties, respectively.

Energy Bin [GeV/n]	C/O
10.0–12.6	$0.997 \pm 0.005^{+0.039}_{-0.019}$
12.6–15.8	$0.967 \pm 0.005^{+0.013}_{-0.034}$
15.8–20.0	$0.939 \pm 0.006^{+0.010}_{-0.026}$
20.0–25.1	$0.935 \pm 0.006^{+0.009}_{-0.010}$
25.1–31.6	$0.927 \pm 0.008^{+0.014}_{-0.006}$
31.6–39.8	$0.911 \pm 0.009^{+0.020}_{-0.006}$
39.8–50.1	$0.896 \pm 0.010^{+0.033}_{-0.009}$
50.1–63.1	$0.894 \pm 0.011^{+0.016}_{-0.007}$
63.1–79.4	$0.877 \pm 0.013^{+0.032}_{-0.008}$
79.4–100.0	$0.909 \pm 0.016^{+0.031}_{-0.008}$
100.0–125.9	$0.887 \pm 0.019^{+0.038}_{-0.004}$
125.9–158.5	$0.866 \pm 0.022^{+0.061}_{-0.010}$
158.5–199.5	$0.866 \pm 0.026^{+0.055}_{-0.008}$
199.5–251.2	$0.874 \pm 0.031^{+0.043}_{-0.014}$
251.2–316.2	$0.903 \pm 0.038^{+0.031}_{-0.045}$
316.2–398.1	$0.910 \pm 0.045^{+0.055}_{-0.056}$
398.1–501.2	$0.848 \pm 0.050^{+0.064}_{-0.064}$
501.2–631.0	$0.843 \pm 0.058^{+0.051}_{-0.064}$
631.0–794.3	$0.880 \pm 0.071^{+0.039}_{-0.061}$
794.3–1000.0	$0.866 \pm 0.084^{+0.063}_{-0.085}$
1000.0–1258.9	$0.891 \pm 0.097^{+0.068}_{-0.092}$
1258.9–2166.7	$1.012 \pm 0.141^{+0.065}_{-0.115}$

[S1] Y. Akaike (CALET), in *Proceedings of Science (ICRC2015) 613* (2015).
[S2] G. D'Agostini, Nucl. Instr. and Meth. A **362**, 487 (1995).
[S3] T. Adye, (2011), arXiv:1105.1160.
[S4] R. Brun and R. Rademarkers, Nucl. Instr. and Meth. A **389**, 81 (1997).
[S5] M. Aguilar *et al.* (AMS), Phys. Rev. Lett. **119**, 251101 (2017).
[S6] J. J. Engelmann *et al.* (CREAM), Astron. Astrophys. **233**, 96 (1990).
[S7] D. Müller *et al.*, Astrophys. J. **374**, 356 (1991).
[S8] O. Adriani *et al.* (PAMELA), Astrophys. J. **93**, 791 (2014).
[S9] E. Atkin *et al.* (NUCLEON), Journal of Cosmology and Astroparticle Physics **2017**, 020 (2017).
[S10] M. Simon *et al.*, Astrophys. J. **239**, 712 (1980).
[S11] A. Panov *et al.* (ATIC), Bull. Russian Acad. Sci. **73**, 564 (2009).
[S12] M. Ave *et al.* (TRACER), Astrophys. J. **678**, 262 (2008).
[S13] H. S. Ahn *et al.* (CREAM), Astrophys. J. **707**, 593 (2009).